

# Reconstructing wave profiles from inundation data

S.W. Funke<sup>a,\*</sup>, P.E. Farrell<sup>b,a</sup>, M.D. Piggott<sup>c</sup>

<sup>a</sup>*Biomedical Computing, Simula Research Laboratory, 1364 Fornebu, Norway*

<sup>b</sup>*Mathematical Institute, University of Oxford, OX2 6GG, UK*

<sup>c</sup>*Department of Earth Science and Engineering, Imperial College London, London, SW7 2AZ, UK*

---

## Abstract

This paper applies variational data assimilation to inundation problems governed by the shallow water equations with wetting and drying. The objective of the assimilation is to recover an unknown time-varying wave profile at an open ocean boundary from inundation observations. This problem is solved with derivative-based optimisation and an adjoint wetting and drying scheme to efficiently compute sensitivity information. The capabilities of this approach are demonstrated on an idealised sloping beach setup in which the profile of an incoming wave is reconstructed from wet/dry interface observations. The method is robust to noise in the observations if a regularisation term is added to the optimisation objective. Finally, the method is applied to a laboratory experiment of the Hokkaido-Nansei-Oki tsunami, where the wave profile is reconstructed with a relative  $L^\infty$  error of less than 1%.

*Keywords:* wetting and drying, data assimilation, finite element method, adjoint wetting and drying, sensitivity analysis

---

## 1. Introduction

Wetting and drying plays an important role in coastal research for the study of tsunamis (Kowalik et al., 2005), storm surge hazards (Westerink et al., 2008), tidal flats and river estuaries (Zhang et al., 2009; Xue and Du, 2010; Kärnä et al., 2011), and other flooding events (Song et al., 2011). Many algorithms have been proposed for the simulation of wetting and drying

---

\*Corresponding author

*Email address:* `simon@simula.no` (S.W. Funke)

7 processes, both for the shallow-water equations (Medeiros and Hagen (2013)  
8 and the references therein, Zhao et al. (2014); Vater et al. (2015); Barros  
9 et al. (2015)) and for the Navier-Stokes equations (Funke et al., 2011; Candy,  
10 2017).

11 In addition to the pure simulation of wetting and drying problems, it is  
12 often desirable to study the sensitivity of the result with respect to changes  
13 in the input parameters such as initial and boundary conditions. The key  
14 for the efficient computation of these sensitivities is the adjoint approach  
15 (Cacuci, 1981; Errico, 1997; Gunzburger, 2003). In the context of shallow  
16 water modelling without wetting and drying, adjoint models have been in-  
17 troduced by (Courtier and Talagrand, 1990) and used in data assimilation  
18 (Bagchi and Brummelhuis, 1994; Gejadze and Copeland, 2005; Chen and  
19 Navon, 2009) and parameter identification (Ding and Wang, 2005), to wave  
20 and flood control (Kawahara and Kawasaki, 1990; Sanders and Katopodes,  
21 1996, 2000; Ding and Wang, 2006; Samizo and Kawahara, 2011). Blaise  
22 et al. (2013) successfully reconstructed the initial condition for a tsunami  
23 simulation from buoy measurements, but also emphasized the importance of  
24 including wetting and drying in the adjoint model as future work.

25 The main contribution of this paper is the derivation and development  
26 of an adjoint model for the shallow water equations with wetting and drying  
27 based on the wetting and drying scheme proposed by Kärnä et al. (2011).  
28 The adjoint model is used to compute the sensitivity of the wet/dry interface  
29 with respect to boundary conditions at a computational cost equivalent to one  
30 linearised shallow water solve. This adjoint model is then utilised in a data  
31 assimilation algorithm to reconstruct the incoming wave height to match  
32 an observed wet/dry interface. Different test problems with and without  
33 added noise show that the reconstruction algorithm works robustly. The  
34 performance of the reconstruction is observed to depend on the “complexity”  
35 of the incoming wave, but not on the numerical discretisation.

## 36 2. Shallow water model with wetting and drying

### 37 2.1. Continuous formulation

The non-linear shallow water equations with appropriate initial and boundary conditions are considered here in the form

$$\frac{\partial u}{\partial t} + (u \cdot \nabla)u + g\nabla\eta = -\frac{c_f(H)}{H}\|u\|u \quad \text{in } \Omega \times (0, T), \quad (1a)$$

$$\frac{\partial \eta}{\partial t} + \nabla \cdot (Hu) = 0 \quad \text{in } \Omega \times (0, T), \quad (1b)$$

$$u \cdot n = 0 \quad \text{on } \partial\Omega_S \times (0, T), \quad (1c)$$

$$\eta = \eta_D \quad \text{on } \partial\Omega_D \times (0, T), \quad (1d)$$

$$u = u_0, \quad \eta = \eta_0 \quad \text{at } \Omega \times \{0\}, \quad (1e)$$

where  $\Omega \subset \mathbb{R}^2$  is the domain of interest,  $T$  is the final time,  $u$  is the unknown depth-averaged velocity,  $\eta$  is the unknown free-surface displacement,  $h$  describes the static bathymetry,  $H = \eta + h$  is the total water depth,  $u_0$  and  $\eta_0$  are the initial conditions, and  $n$  is the normal vector on the boundary. The water height variables are sketched in figure 1a. The domain boundary is divided into  $\partial\Omega_S$ , where a no-normal flow condition is imposed, and  $\partial\Omega_D$ , where a Dirichlet boundary condition prescribes the free-surface displacement  $\eta_D$ . The remaining parameters are the gravitational force  $g$  and the friction coefficient in the Chézy-Manning formulation (Hervouet, 2007)

$$c_f(H) = \frac{g\mu^2}{H^{1/3}},$$

38 where  $\mu$  is the user specified Manning coefficient.

39 In its standard form, the shallow water equations do not account for wet-  
40 ting and drying processes. With wetting and drying, the domain  $\Omega$  becomes  
41 an unknown variable itself, described by all points where the total water-level  
42 is positive. Hence, equations (1) are extended by the domain equation

$$\Omega(t) = \{(x, y) : H(x, y, t) > 0\}. \quad (2)$$

43 The numerical treatment of wetting and drying is challenging, and various ex-  
44 tensions have been proposed and are reviewed in Medeiros and Hagen (2013).  
45 A classical approach is to mark individual mesh elements in the computa-  
46 tional domain as wet or dry and remove dry elements from the time step

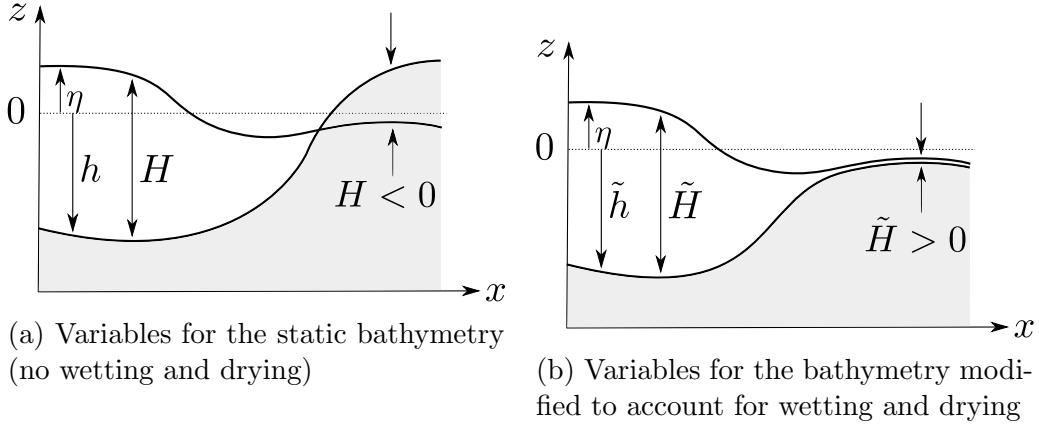


Figure 1: The modified water depth variables for the wetting and drying scheme by Kärnä et al. (2011).

47 computation. However, the elemental wet/dry conditions usually involve  
 48 discontinuous functions, which complicates the development of the adjoint  
 49 system. This can be seen in the work of Miyaoka and Kawahara (2008),  
 50 where the wetting and drying algorithm was ignored in the adjoint com-  
 51 putation; instead, the adjoint shallow water equations without wetting and  
 52 drying were solved only in the wet area. Such an approach cannot provide  
 53 the sensitivity of the wet/dry interface, which is needed here for the data  
 54 assimilation. Therefore, we use an alternative wetting and drying algorithm  
 55 proposed by Kärnä et al. (2011), motivated by the fact that their numerical  
 56 scheme is continuous and differentiable (though for some problems BFGS  
 57 can successfully be applied to non-smooth functions (Stewart et al., 2013)).

The wetting and drying algorithm is based on the idea of replacing the static bathymetry  $h$  with a dynamic bathymetry  $\tilde{h}$ , which moves such that the water level remains always positive. This dynamic bathymetry is defined as

$$\tilde{h}(x, t) := h + f(H),$$

58 where  $f$  is a smooth function that ensures the positiveness of the total water  
 59 depth, that is:

$$\tilde{H} := \eta + \tilde{h} > 0. \quad (3)$$

60 The modified variables for the dynamic bathymetry approach are sketched  
 61 in figure 1b. For the function  $f$ , Kärnä et al. (2011) suggest a smooth ap-

62 proximation of the maximum operator:

$$f(H) := \frac{1}{2} \left( \sqrt{H^2 + \alpha^2} - H \right) \approx \max(0, -H). \quad (4)$$

63 This function choice, plotted in figure 2a, is also used in this work. The  
 64 parameter  $\alpha > 0$  controls the accuracy of the approximation to the max  
 65 operator. Kärnä et al. (2011) provides a guideline for determining a suitable  
 66 estimate for this parameter:

$$\alpha := d_e \|\nabla h\|, \quad (5)$$

67 where  $d_e$  is a typical length scale of a representative element in the compu-  
 68 tational mesh. By ensuring that  $\alpha \rightarrow 0$  as the mesh size goes to zero, this  
 69 ensures consistency of the discretisation with the nonsmooth equations.

70 The modified shallow water equations that include wetting and drying  
 71 are obtained from the original equations (1) by replacing the total depth  
 72  $H$  with its dynamic variant  $\tilde{H}$  and including the time derivative of the dy-  
 73 namic bathymetry  $\tilde{h}$  in the continuity equation to account for the temporal  
 74 variability of the bathymetry:

$$\begin{aligned} \frac{\partial u}{\partial t} + (u \cdot \nabla)u + g\nabla\eta &= -\frac{c_f(\tilde{H})}{\tilde{H}}\|u\|u \quad \text{in } \Omega \times (0, T), \\ \frac{\partial \eta}{\partial t} + \frac{\partial \tilde{h}}{\partial t} + \nabla \cdot (\tilde{H}u) &= 0 \quad \text{in } \Omega \times (0, T), \\ u \cdot n &= 0 \quad \text{on } \partial\Omega_S \times (0, T), \\ \eta &= \eta_D \quad \text{on } \partial\Omega_D \times (0, T), \\ u = u_0, \quad \eta &= \eta_0 \quad \text{at } t = 0. \end{aligned} \quad (6)$$

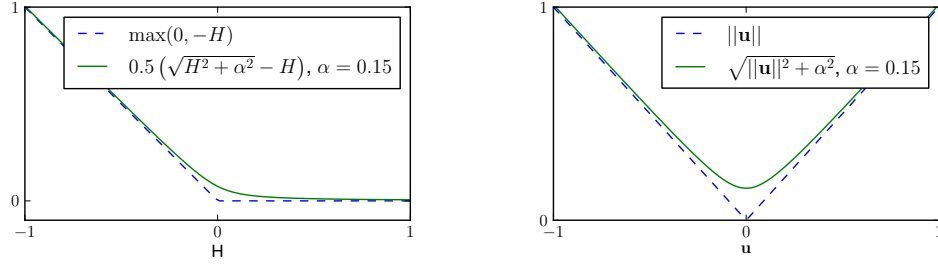
To avoid non-differentiable functions in the continuous formulation, the norm operator in (6) is replaced by a smooth approximation:

$$\|u\| \approx \sqrt{\|u\|^2 + \alpha^2},$$

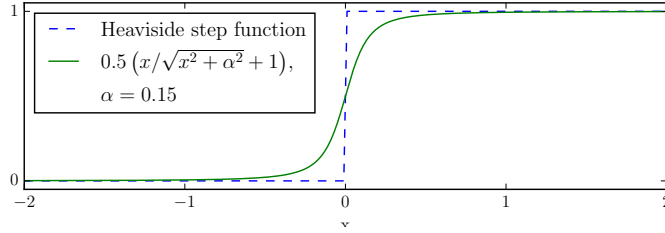
75 with the same  $\alpha$  constant as above. A plot of this approximation function is  
 76 given in figure 2b.

## 77 2.2. Spatial discretisation

78 The modified shallow water equations (6) are discretised in space with  
 79 a mixed continuous-discontinuous finite element method. A general intro-  
 80 duction to discontinuous Galerkin methods can be found in Hesthaven and  
 81 Warburton (2008).



(a) Smooth approximation of  $\max(0, -H)$ , used to enforce a positive water level in equation (3) (b) Smooth approximation of the norm,  $||\mathbf{u}||$ , used in the drag term of the momentum equation (1a)



(c) Smooth approximation of the Heaviside step function (11), used in the functional of interest as an indicator function for dry areas. The approximation is equivalent to  $f'(x) + 1$ , with  $f$  defined in equation (4)

Figure 2: The non-smooth functions in the wetting and drying scheme are replaced with these continuously differentiable approximations. The approximation is controlled by  $\alpha$ .

The discrete function spaces are constructed with the P1<sub>DG</sub>-P2 finite element pair, that is the velocity components are piecewise linear on each mesh triangle and discontinuous on the mesh edges, while the pressure is piecewise quadratic and continuous (Cotter et al., 2009; Comblen et al., 2010). Let  $V$  and  $W$  denote the associated function spaces for the velocity and free-surface displacement fields, respectively. The weak formulation is obtained by multiplying the two partial differential equations in (6) with test functions  $\Psi \in V$  and  $\Phi \in W$  and integrating over the domain  $\Omega$ . The resulting discretised variational problem is to find  $u \in V, \eta \in W$  such that  $\forall \Psi \in V, \Phi \in W$ :

$$\begin{aligned} & \left\langle \frac{\partial u}{\partial t}, \Psi \right\rangle_{\Omega} + \langle (u \cdot \nabla)u, \Psi \rangle_{\Omega} - \sum_{e \in E} (\langle \{u^+\} \llbracket u \rrbracket, \Psi^+ \rangle_e - \langle \{u^-\} \llbracket u \rrbracket, \Psi^- \rangle_e) \\ & + \langle g \nabla \eta, \Psi \rangle_{\Omega} - g \langle \eta - \eta_D, \Psi \cdot n \rangle_{\partial \Omega_D} = - \left\langle \frac{c_f(\tilde{H})}{\tilde{H}} \|u\| u, \Psi \right\rangle_{\Omega}, \end{aligned} \quad (7a)$$

$$\left\langle \frac{\partial \tilde{H}}{\partial t}, \Phi \right\rangle_{\Omega} - \langle (\tilde{H}u), \nabla \Phi \rangle_{\Omega} + \langle \tilde{H}u \cdot n, \Phi \rangle_{\partial \Omega \setminus \partial \Omega_S} = 0. \quad (7b)$$

Here,  $E$  denotes the interior mesh facets and the superscripts  $+$  and  $-$  are used to distinguish between the two facet values for the discontinuous functions.  $\{u\}$  represents the downwind value of  $u$ , i.e.:

$$\{u\} := \begin{cases} u \cdot n & \text{if } u \cdot n < 0, \\ 0 & \text{otherwise,} \end{cases}$$

and  $\llbracket u \rrbracket$  denotes the jump of  $u$  across the facet side:

$$\llbracket u \rrbracket := u^+ - u^-.$$

82 The above formulation includes a simple upwinding scheme for the velocity  
83 advection term, which is obtained by integrating by parts twice, and replacing  
84 the advected velocity at the inflow facets with the upwind velocity. The no-  
85 normal flow boundary condition has been weakly enforced by neglecting the  
86 surface integrals associated with the domain boundary  $\partial \Omega_S$  in equation (7b).  
87 Similarly, the pressure term in the momentum equation (7a) is integrated  
88 twice by parts to weakly enforce the Dirichlet boundary condition on  $\partial \Omega_D$ .

89 As discussed in Kärnä et al. (2011), volume conservation is only sat-  
90 isfied if the integrals featuring the continuity equation (7b) are evaluated

91 accurately. Since  $\tilde{H}$  is not a polynomial function, standard quadrature rules  
 92 cannot evaluate these integrals exactly. Section 2.4 investigates this issue and  
 93 shows how the quadrature degree affects the volume conservation. Another  
 94 difficulty is to ensure that  $\tilde{H}$  is positive everywhere also at the discrete level.  
 95 Kärnä et al. (2011) uses piecewise linear elements for  $\tilde{H}$  and exploits the fact  
 96 that functions based on linear finite elements take their extrema at vertices.  
 97 Therefore a nodewise projection for  $\tilde{H}$  ensures a domain-wide positive water  
 98 level. To circumvent this problem for the quadratic elements used here to  
 99 represent water depth,  $\tilde{H}$  itself is never stored as a discrete function, but is  
 100 instead reevaluated for each quadrature point using equation (3).

### 101 2.3. Temporal discretisation

102 Following Kärnä et al. (2011), the weak equations (7) are discretised in  
 103 time using the diagonally implicit Runge-Kutta scheme DIRK (2,3,2) (Ascher  
 104 et al., 1997, §2.5). This is a second-order, L- and A-stable scheme (Hairer  
 105 and Wanner, 1996), which ensures accuracy while allowing large time steps  
 106 in the time integration.

The continuous time period is split into discrete levels with associated  
 time steps  $\Delta t$ . For each time level, DIRK schemes solve a sequence of stages,  
 each of which requires solving a system of non-linear equations. For brevity,  
 we write the weak equations (7) in the shortened form:

$$\begin{aligned} \left\langle \frac{\partial u}{\partial t}, \Psi \right\rangle_{\Omega} &= S_u(\eta, u), \\ \left\langle \frac{\partial \tilde{H}}{\partial t}, \Phi \right\rangle_{\Omega} &= S_{\eta}(\eta, u). \end{aligned}$$

107 Let the superscript  $n$  denote the time level and superscripts  $i$  and  $j$  denote  
 108 DIRK stages. The computation of time level  $n$  involves the following steps:

- For each stage  $i = 1, \dots, s$  solve the following non-linear system for  
 intermediate solutions  $u^i$  and  $\eta^i$ :

$$\begin{aligned} \langle u^i, \Psi \rangle_{\Omega} &= \langle u^{n-1}, \Psi \rangle_{\Omega} + \Delta t \sum_{j=1}^i a_{i,j} S_u(\eta^j, u^j), \\ \langle \tilde{H}^i, \Phi \rangle_{\Omega} &= \langle \tilde{H}^{n-1}, \Phi \rangle_{\Omega} + \Delta t \sum_{j=1}^i a_{i,j} S_{\eta}(\eta^j, u^j). \end{aligned}$$



Each stage has an associated time level of  $t^i = t^n + c_i \Delta t$  which is used to evaluate the forcing terms. The coefficients  $a_{i,j}$  and  $c_i$  depend on the specific Runge-Kutta method and are defined below.

- A final stage linearly combines the intermediate solutions to obtain the solution at the next time level  $u^n$  and  $\eta^n$ :

$$\begin{aligned}\langle u^n, \Psi \rangle_\Omega &= \langle u^{n-1}, \Psi \rangle_\Omega + \Delta t \sum_{j=1}^s b_j S_u(\eta^j, u^j), \\ \langle \tilde{H}^n, \Phi \rangle_\Omega &= \langle \tilde{H}^{n-1}, \Phi \rangle_\Omega + \Delta t \sum_{j=1}^s b_j S_\eta(\eta^j, u^j).\end{aligned}$$

Again, the coefficients  $b_j$  depend on the specific Runge-Kutta method used.

In general, the Runge-Kutta coefficients  $a_{ij}$ ,  $b_j$  and  $c_i$  are defined compactly in the form of a Butcher tableau:

$$\begin{array}{c|ccc} c_1 & a_{1,1} & & \\ c_2 & a_{2,1} & a_{2,2} & \\ \vdots & \vdots & \vdots & \ddots \\ c_s & a_{s,1} & a_{s,2} & \dots a_{s,s} \\ \hline & b_1 & b_2 & \dots b_s \end{array}$$

The Butcher tableau for the DIRK (2,3,2) scheme used in this work is given by (Ascher et al., 1997, §2.6):

$$\begin{array}{c|cc} \gamma & \gamma & \\ 1 & 1 - \gamma & \gamma \\ \hline & 1 - \gamma & \gamma \end{array}$$

with  $\gamma := (2 - \sqrt{2})/2$ .

#### 2.4. Verification

The shallow water model with wetting and drying was implemented using the FEniCS framework (Logg et al., 2011). The implementation was verified with the commonly used ‘Thacker’ test case for which an analytical solution is known (Thacker, 1981).

The Thacker test considers an undamped wave in a flat, bowl shaped basin where wetting and drying occurs on its sides. The domain consists of a circular basin with a parabolic depth

$$h(x, y) := h_c \left( 1 - \frac{x^2 + y^2}{L^2} \right),$$

where  $L$  and  $h_c$  are positive constants describing the basin's radius and depth at its centre, respectively. The analytical solution satisfies the shallow water equations with wetting and drying, (1) and (2), without bottom friction, that is  $\mu = 0$  and is:

$$u_{\text{exact}}(x, y, t) := \frac{\omega A \sin(\omega t)}{2(1 - A \cos(\omega t))} \begin{pmatrix} x \\ y \end{pmatrix},$$

$$\eta_{\text{exact}}(x, y, t) := h_c \left( \frac{\sqrt{1 - A^2}}{1 - A \cos \omega t} - 1 - \frac{x^2 + y^2}{L^2} \left( \frac{1 - A^2}{(1 - A \cos \omega t)^2} - 1 \right) \right),$$

with

$$\omega^2 := \frac{8gh_c}{L^2}, \quad A := \frac{(h_c + \eta_c)^2 - h_c^2}{(h_c + \eta_c)^2 + h_c^2},$$

128 and  $\eta_c$  is the maximum free-surface displacement at the basin's centre. The  
 129 parameters for the numerical tests were chosen to be consistent with Balzano  
 130 (1998):  $L = 430.62$  km,  $h_c = 50$  m,  $\eta_c = 2$  m and a gravity magnitude of  
 131  $g = 9.81$  m/s<sup>2</sup>. This results in a periodic free-surface oscillation with a 12 h  
 132 period, see figure 3.

133 The Thacker test case was numerically solved on four meshes with in-  
 134 creasing resolution (figure 4). To ensure that the domain is sufficiently large  
 135 to capture the wetting and drying process, the computational domain con-  
 136 sists of a circle with radius 496.20 km, in accordance to Kärnä et al. (2011).  
 137 The simulation was carried out for 24 h with a time step of 300 s. This time  
 138 step is small enough to ensure that the spatial error dominates the temporal  
 139 discretisation error: performing the convergence analysis with a time step of  
 140 150 s resulted in similar convergence results. The smoothness constant  $\alpha$  is  
 141 estimated using equation (5) and yields  $\alpha \approx 2.4$  m for the finest mesh. Sub-  
 142 sequent numerical experiments showed that this value can further be reduced  
 143 to  $\alpha = 1.8$  m without compromising the stability of the simulation. Hence,  
 144 this reduced value was used for the finest mesh, and linearly increased with  
 145 the mesh element sizes for the coarser meshes (that is  $\alpha = 1.8, 3.6, 5.4, 7.2$  m  
 146 for the 10, 20, 30, 40 km element size meshes, respectively).

The model implementation was verified by repeating the convergence test performed by Kärnä et al. (2011) and comparing the resulting order of convergence. The error measure is defined as:

$$\mathcal{E} := \int_0^T \|\tilde{\eta} - \tilde{\eta}_{\text{exact}}\|_{L^2(\Omega)} dt,$$

147 where  $\tilde{\eta} := \tilde{H} - h$  and  $\tilde{\eta}_{\text{exact}} := \max(\eta_{\text{exact}}, -h)$  are the numerical and analytical  
 148 solutions that take the bathymetry into account. The numerical errors  
 149 for the four meshes are plotted in figure 5. The average convergence rate is  
 150 1.46, which is consistent with the observed order of convergence of 1.47 in  
 151 Kärnä et al. (2011).

## 152 2.5. Volume conservation

153 As discussed in section 2.2, it has to be assessed whether, and to what  
 154 extent, the finite quadrature rule affects volume conservation. Furthermore,  
 155 volume conservation might be affected by the tolerance setting of the Newton  
 156 solver which is used to solve the non-linear problem at each timestep.

To study the conservation of volume, the Thacker test case introduced in the previous section was used. It consists of a closed domain and therefore the fluid volume should remain constant throughout time. Using the setup with the coarsest mesh from the previous section, the Thacker test case was solved for a combination of different quadrature degrees and Newton tolerances. For each combination, the maximum relative error in the volume conservation was computed as

$$\mathcal{E}_V := \max_{t \in (0, T)} \left| \frac{V(0) - V(t)}{V(0)} \right|,$$

157 where  $V(t) := \int_{\Omega} \tilde{H}(t) dx$  is the total fluid volume at a time  $t$ .

158 The results of these tests are listed in table 1. The volume conserva-  
 159 tion error is largely dominated by the tolerance of the Newton solver while  
 160 the quadrature degree has only marginal influence. The numerical simula-  
 161 tions that follow use a quadrature degree of 20 and a relative Newton solver  
 162 tolerance of  $10^{-9}$ .

## 163 2.6. Validation

164 The validation of the forward model is outside the scope of this work.  
 165 However, it should be noted that the wetting and drying scheme employed

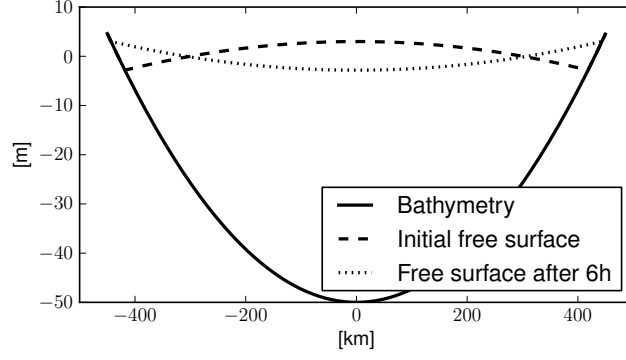
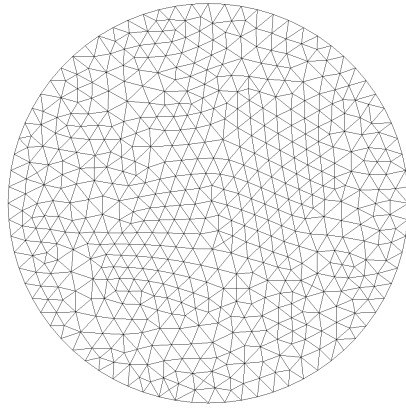


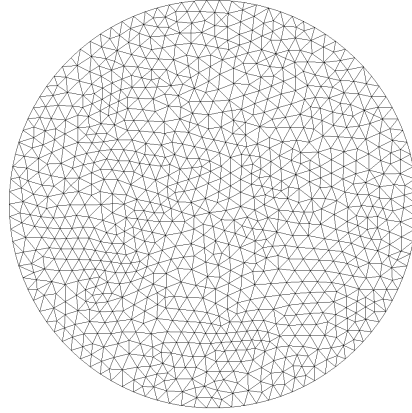
Figure 3: The setup of the Thacker problem. The free-surface oscillates with a 12 h period, while wetting and drying occurs at the sides of the basin.

Quadrature degree	Newton tolerance	Relative volume error $\mathcal{E}_V$
4	$10^{-6}$	$1.3 \times 10^{-8}$
4	$10^{-9}$	$5.7 \times 10^{-12}$
4	$10^{-12}$	$4.5 \times 10^{-15}$
20	$10^{-6}$	$1.3 \times 10^{-8}$
20	$10^{-9}$	$5.7 \times 10^{-12}$
20	$10^{-12}$	$2.8 \times 10^{-15}$
121	$10^{-6}$	$1.3 \times 10^{-8}$
121	$10^{-9}$	$5.7 \times 10^{-12}$
121	$10^{-12}$	$2.7 \times 10^{-15}$

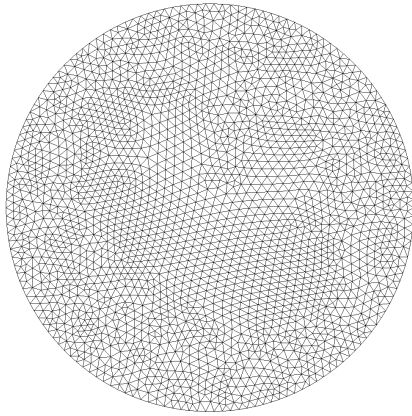
Table 1: The maximum relative volume conservation error over 24 h on the coarsest mesh (figure 4a) for different quadrature degrees and relative Newton solver tolerances.



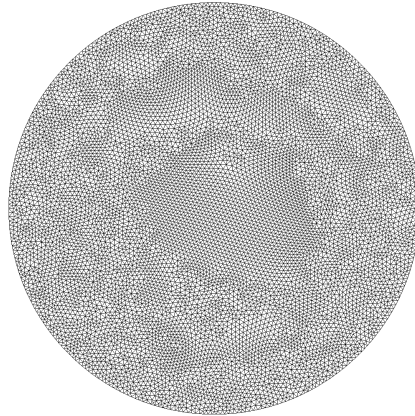
(a) 40 km mesh resolution



(b) 30 km mesh resolution



(c) 20 km mesh resolution



(d) 10 km mesh resolution

Figure 4: The four meshes (generated with Gmsh (Geuzaine and Remacle, 2009)) used for the Thacker test case to determine the spatial convergence rate of the shallow water model with wetting and drying.

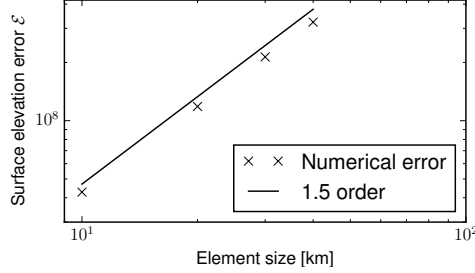


Figure 5: Spatial discretisation errors computed from the four meshes shown in figure 4. The average rate of convergence is 1.46; Kärnä et al. (2011) observed an order of 1.47.

166 here has previously been applied to the Scheldt estuary and the North Sea,  
 167 and validated against tidal stations with good results in Kärnä et al. (2011);  
 168 Gourgue (2011); de Brye et al. (2012, 2010).

### 169 3. The data assimilation problem

#### 170 3.1. Formulation as an optimisation problem

171 This section formulates the problem of reconstructing the profile of an in-  
 172 coming wave from inundation observations as an optimisation problem con-  
 173 strained by the shallow water equations. This will allow us to apply tech-  
 174 niques such as gradient-based optimisation methods and the adjoint model  
 175 to efficiently solve the data assimilation problem.

176 The goal quantity that we aim to minimise measures the misfit between an  
 177 observed and the simulated wet/dry interface at all time levels. For that, we  
 178 map the simulated water height  $\eta$  to an indicator function which approaches  
 179 1 in dry and 0 in wet areas. By noting that  $H \geq 0$  in wet and  $H < 0$  in dry  
 180 areas (see figure 1a), this indicator function is defined as  $-\mathcal{H}(\eta + h)$  where  
 181  $\mathcal{H}$  is a smooth approximation of the Heaviside step function:

$$\mathcal{H}(x) := \frac{1}{2} \left( \frac{x}{\sqrt{x^2 + \alpha^2}} + 1 \right) \approx \begin{cases} 0 & \text{if } x < 0, \\ 1 & \text{otherwise,} \end{cases} \quad (11)$$

182 where  $\alpha$  controls the smoothness of the approximation. A plot of this ap-  
 183 proximation is given in figure 2c. Given some observations  $d$  of a wet/dry  
 184 interface (that is,  $d$  is an time-varying function that approaches 1 at dry and

0 at wet points), we define the goal quantity as

$$J(\eta, \eta_D) := \frac{1}{2} \int_0^T \int_{\Omega} |-\mathcal{H}(\eta + h) - d|^2 \, dx \, dt + \frac{\beta}{2} \int_0^T \int_{\partial\Omega_D} \left| \frac{\partial \eta_D}{\partial t} \right|^2 \, dx \, dt. \quad (12)$$

The first term is a tracking-type functional and quantifies the discrepancy between simulated and observed wet/dry interfaces, while the second term is a Tikhonov regularisation term that enforces temporal smoothness in the boundary displacement: a larger  $\beta$  value results in smoother boundary displacement in the reconstructed profile.

The optimisation parameters are the Dirichlet boundary values  $\eta_D$  at each time level in the shallow water equations (6). Note that the computation of the Runge-Kutta stages requires the Dirichlet boundary values at intermediate time levels, see section 2.3. These values are obtained by linearly interpolating the boundary values from the two neighbouring time levels. For simplicity, the numerical examples presented here assume that the boundary values only vary in time and are constant in space. For spatially varying boundary conditions, the functional 12 would need to be extended by an additional spatial regularisation term. It should be highlighted that the computational expense is not expected to increase significantly for spatially varying boundary controls, since the adjoint approach yields the functional gradient at a cost that is essentially independent to the number of control variables.

We can now state the data assimilation problem as an optimisation problem with the shallow water equations as a constraint:

$$\begin{aligned} \min_{\eta_D, u, \eta} \quad & J(\eta, \eta_D) \quad \text{subject to} \\ \frac{\partial u}{\partial t} + (u \cdot \nabla)u + g\nabla\eta &= -\frac{c_f(\tilde{H})}{\tilde{H}} \|u\|u \quad \text{in } \Omega \times (0, T), \\ \frac{\partial \eta}{\partial t} + \frac{\partial \tilde{h}}{\partial t} + \nabla \cdot (\tilde{H}u) &= 0 \quad \text{in } \Omega \times (0, T), \\ u \cdot n &= 0 \quad \text{on } \partial\Omega_S \times (0, T), \\ \eta &= \eta_D \quad \text{on } \partial\Omega_D \times (0, T), \\ u = u_0, \quad \eta &= \eta_0 \quad \text{at } \Omega \times \{0\}. \end{aligned} \quad (13)$$

### 3.2. Adjoint model

In order to efficiently solve the optimisation problem (13), we need to apply gradient-based optimisation methods which require the derivative of

209 the goal quantity with respect to the optimisation parameters,  $dJ/d\eta_D$ . This  
 210 derivative can be computed by solving the adjoint equations at computational  
 211 cost of approximately one solution of a linearised shallow water problem.

**Proposition 1.** *The strong adjoint equations of the shallow water equations with wetting and drying are: find  $\lambda_u$  and  $\lambda_\eta$  such that*

$$\begin{aligned}
 & -\frac{\partial \lambda_u}{\partial t} + (\nabla u)^* \lambda_u - (u \cdot \nabla) \lambda_u - (\nabla \cdot u) \lambda_u \\
 & - \tilde{H} \nabla \lambda_\eta + \frac{c_f(\tilde{H})}{\tilde{H}} (\|u\| \lambda_u + \lambda_u \cdot u \|u\|^{-1} u) = \frac{\partial J}{\partial u} \quad \text{in } \Omega \times (0, T), \\
 & -\mathcal{H}(H) \frac{\partial \lambda_\eta}{\partial t} - \mathcal{H}(H) u \cdot \nabla \lambda_\eta - g \nabla \cdot \lambda_u - \frac{4c_f(\tilde{H})}{3\tilde{H}^2} \mathcal{H}(H) \|u\| u \cdot \lambda_u = \frac{\partial J}{\partial \eta} \quad \text{in } \Omega \times (0, T), \\
 & \lambda_u \cdot n = 0 \quad \text{on } \partial\Omega_S \times (0, T), \\
 & \lambda_\eta = 0 \quad \text{on } \partial\Omega_D \times (0, T), \\
 & \lambda_u = 0, \quad \lambda_\eta = 0 \quad \text{at } \Omega \times \{T\}.
 \end{aligned} \tag{14}$$

212 We prove this statement after the following theorem. Note that the initial  
 213 time condition in the forward problems becomes a final time condition in the  
 214 adjoint problem and that the adjoint problem has homogeneous boundary  
 215 conditions.

**Proposition 2.** *The weak formulation of the adjoint shallow water equations with wetting and drying is: Find  $\lambda_u \in V$  and  $\lambda_\eta \in W$  such that for all  $\Psi \in V$  and  $\Phi \in W$ :*

$$\begin{aligned}
 & \left\langle \frac{\partial \Psi}{\partial t}, \lambda_u \right\rangle_\Omega + \langle (\Psi \cdot \nabla) u + (u \cdot \nabla) \Psi, \lambda_u \rangle_\Omega \\
 & - \sum_{e \in E} (\langle \{\Psi^+\}_{u^+} \llbracket u \rrbracket + u^+ \rangle \llbracket \Psi \rrbracket, \lambda_u^+ \rangle_e) \\
 & - \sum_{e \in E} (\langle \{\Psi^-\}_{u^-} \llbracket u \rrbracket - u^- \rangle \llbracket \Psi \rrbracket, \lambda_u^- \rangle_e) \\
 & + \left\langle \frac{c_f(\tilde{H})}{\tilde{H}} (u \cdot \Psi \|u\|^{-1} u + \|u\| \Psi), \lambda_u \right\rangle_\Omega \\
 & - \left\langle (\tilde{H} \Psi), \nabla \lambda_\eta \right\rangle_\Omega + \left\langle \tilde{H} \Psi \cdot n, \lambda_\eta \right\rangle_{\partial\Omega \setminus \partial\Omega_S} = \frac{\partial J}{\partial u}
 \end{aligned} \tag{15}$$



and

$$\begin{aligned} & \left\langle \partial \frac{\mathcal{H}(H)\Phi}{\partial t}, \lambda_\eta \right\rangle_\Omega - \langle (\mathcal{H}(H)\Phi u, \nabla \lambda_\eta) \rangle_\Omega + \langle \mathcal{H}(H)\Phi u \cdot n, \lambda_\eta \rangle_{\partial\Omega \setminus \partial\Omega_S} \\ & + \langle g \nabla \Phi, \lambda_u \rangle_\Omega - g \langle \Phi, \lambda_u \cdot n \rangle_{\partial\Omega_D} - \left\langle \frac{4c_f(\tilde{H})}{3\tilde{H}^2} \mathcal{H}(H)\Phi \|u\|u, \lambda_u \right\rangle_\Omega = \frac{\partial J}{\partial \eta} \end{aligned} \quad (16)$$

216 where  $\{\Psi\}_u$  denotes the derivative of the (smoothed) upwind velocity at  $u$  in  
217 direction  $\Psi$ .

218 *Proof.* For the derivation of the general adjoint equations, we refer to Hinze  
219 et al. (2009). The adjoint equations are obtained in two steps. First, we form  
220 the linearised operator of the semi-discrete wetting and drying scheme (7),  
221 which can be written in matrix form as:

$$\begin{pmatrix} \Psi & \Phi \end{pmatrix} \begin{pmatrix} J_{11} & J_{21} \\ J_{12} & J_{22} \end{pmatrix} \begin{pmatrix} \delta u \\ \delta \eta \end{pmatrix} \quad (17)$$

where  $J_{ij}$  are the (bilinear) components of the Jacobian. More specifically,  
 $J_{11}$  is the derivative of (7a) with respect to  $u$  in direction  $\delta u$ :

$$\begin{aligned} J_{11}(\delta u, \Psi) &= \left\langle \frac{\partial \delta u}{\partial t}, \Psi \right\rangle_\Omega + \langle (\delta u \cdot \nabla)u, \Psi \rangle_\Omega + \langle (u \cdot \nabla)\delta u, \Psi \rangle_\Omega \\ &\quad - \sum_{e \in E} (\langle \{\delta u^+\}_{u^+} \llbracket u \rrbracket, \Psi^+ \rangle_e - \langle \{u^+\} \llbracket \delta u \rrbracket, \Psi^+ \rangle_e) \\ &\quad - \sum_{e \in E} (\langle \{\delta u^-\}_{u^-} \llbracket u \rrbracket, \Psi^- \rangle_e - \langle \{u^-\} \llbracket \delta u \rrbracket, \Psi^- \rangle_e) \\ &\quad + \left\langle \frac{c_f(\tilde{H})}{\tilde{H}} \|\delta u\|_u u, \Psi \right\rangle_\Omega + \left\langle \frac{c_f(\tilde{H})}{\tilde{H}} \|u\| \delta u, \Psi \right\rangle_\Omega \end{aligned}$$

where  $\tilde{H}_\eta = \mathcal{H}(\eta + h)$  is the (smoothed) derivative of  $\tilde{H}$  with respect to  $\eta$ ,  
and  $\{\delta u\}_u$  and  $\|\delta u\|_u = u \cdot \delta u \|u\|^{-1}$  denote the derivative of the (smoothed)  
upwind velocity and norm functions at  $u$  in direction  $\delta u$ , respectively.  $J_{12}$  is  
the derivative of (7a) with respect to  $\eta$  in direction  $\delta \eta$ :

$$J_{12}(\delta \eta, \Psi) = \langle g \nabla \delta \eta, \Psi \rangle_\Omega - g \langle \delta \eta, \Psi \cdot n \rangle_{\partial\Omega_D} - \left\langle \frac{4c_f(\tilde{H})}{3\tilde{H}^2} \tilde{H}_\eta \delta \eta \|u\|u, \Psi \right\rangle_\Omega$$

$J_{21}$  is the derivative of (7b) with respect to  $u$  in direction  $\delta u$ :

$$J_{21}(\delta u, \Phi) = - \left\langle (\tilde{H}\delta u), \nabla \Phi \right\rangle_{\Omega} + \left\langle \tilde{H}\delta u \cdot n, \Phi \right\rangle_{\partial\Omega \setminus \partial\Omega_S}.$$

$J_{22}$  is the derivative of (7b) with respect to  $\eta$  in direction  $\delta\eta$ :

$$J_{22}(\delta\eta, \Phi) = \left\langle \frac{\partial \tilde{H}_\eta \delta\eta}{\partial t}, \Phi \right\rangle_{\Omega} - \left\langle (\tilde{H}_\eta \delta\eta u), \nabla \Phi \right\rangle_{\Omega} + \left\langle \tilde{H}_\eta \delta\eta u \cdot n, \Phi \right\rangle_{\partial\Omega \setminus \partial\Omega_S}.$$

222 The variational adjoint operator is now obtained by transposing form (17)

$$\begin{pmatrix} \lambda_u & \lambda_\eta \end{pmatrix} \begin{pmatrix} J_{11} & J_{12} \\ J_{21} & J_{22} \end{pmatrix} \begin{pmatrix} \Psi \\ \Phi \end{pmatrix}. \quad (18)$$

223 Using this bilinear operator with the adjoint forcing term to the right hand  
224 side yields the stated adjoint problem.  $\square$

225 *Proof of Theorem 1.* The strong form of the adjoint shallow water equations  
226 is obtained from its weak formulation, given in theorem 2, and integration by  
227 parts such that the test function have no derivatives in the volume integrals.  
228  $\square$

**Proposition 3.** *The derivative of the functional (12) with respect to the boundary free surface displacement  $\eta_D$  is*

$$J_{\eta_D}(u, \eta, \eta_D; \delta) = - \int_0^T \int_{\partial\Omega_D} g\delta\lambda_u \cdot n dx dt + \beta \int_0^T \int_{\partial\Omega_D} \frac{\partial \eta_D}{\partial t} \delta dx dt \quad (19)$$

229 where  $\delta \in \partial\Omega_D \times (0, T) \rightarrow \mathbb{R}$  is the direction.

230 *Proof.* The weak formulation of the shallow water problem (7) can be written  
231 compactly as  $F(u, \eta, \eta_D; \Phi, \Psi) = 0 \forall (\Phi, \Psi)$ . Then the adjoint approach yields  
232 (see Hinze et al. (2009)):

$$J_{\eta_D}(u, \eta, \eta_D; \delta) = - \frac{\partial F}{\partial \eta_D}(u, \eta, \eta_D; \delta, \lambda_u, \lambda_\eta) + \frac{\partial J}{\partial \eta_D}(u, \eta, \eta_D; \delta). \quad (20)$$

233 Applying (20) to the weak shallow water equations (7) and the functional  
234 (12) yields (19).  $\square$

235 Rather than implementing a solver for the adjoint equations (2) manually,  
 236 it was automatically generated using the FEniCS extension dolfin-adjoint  
 237 (Farrell et al., 2013) (see Naumann (2011) for a detailed description of algo-  
 238 rithmic differentiation or alternatives such as Fang et al. (2013)). dolfin-adjoint  
 239 derives the adjoint model, and the derivative computation, directly from the  
 240 discretised shallow water equations. This has the advantage that the deriva-  
 241 tive is also the derivative of the discrete shallow water model, rather than  
 242 just another approximation of the non-discrete derivative. Without this dis-  
 243 crete consistency, the derivative might be a bad descent direction for the  
 244 optimisation, and one would need to use more robust optimisation methods.

245 The adjoint implementation was verified with the Taylor remainder con-  
 246 vergence test (Navon et al., 1992; Funke, 2012, §2.5.6). Its application to  
 247 an initial example yielded the expected first-order convergence without gra-  
 248 dient information, and second-order convergence with gradient information.  
 249 The Taylor remainder convergence test was then successfully applied to the  
 250 first ten optimisation iterations of all numerical examples in this paper. This  
 251 gives high confidence that the adjoint system and the gradient computation  
 252 are correctly implemented.

## 253 4. Numerical examples

254 This section performs numerical experiments on two data assimilation  
 255 problems with inundation observations. In both cases, the resulting optimi-  
 256 sation problems (13) were solved with the limited memory BFGS method  
 257 with bound support (L-BFGS-B) from SciPy (Byrd et al., 1995; Jones et al.,  
 258 2001). The L-BFGS-B method belongs to the class of quasi-Newton algo-  
 259 rithms that use an approximation of the Hessian matrix based on a limited  
 260 number of functional gradients (here 10).

261 In order to be able to investigate the effectiveness and robustness of the  
 262 wave reconstruction, we apply the method to synthetically generated obser-  
 263 vations of the wet/dry interface. The synthetic observations were obtained  
 264 by first choosing a Dirichlet boundary condition  $\eta_D^{\text{exact}}$ , then solving the shal-  
 265 low water model, and recording the wet/dry interface at each timestep as  
 266  $\mathcal{H}(\eta - h)$ . Using these records as the observations  $d$  in the goal quantity (12)  
 267 guarantees that the chosen Dirichlet boundary condition  $\eta_D^{\text{exact}}$  is a solution  
 268 to the optimisation problem (13).

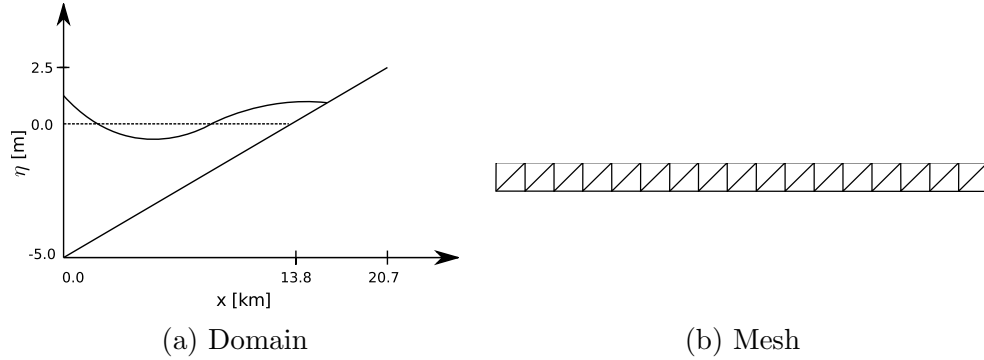


Figure 6: A vertical slice of the setup for the wave profile reconstruction on a sloping beach.

#### 269 4.1. Wave profile reconstruction on a sloping beach

270 The first data assimilation problem consists of a long, thin sloping beach  
 271 with an incoming wave on the deep side. The goal is to reconstruct the wave  
 272 profile based on observations of the wet/dry interface.

273 The computational domain is an adaption of a wetting and drying test  
 274 case considered by Balzano (1998). It consists of a linearly increasing slope  
 275 of 1.2 km width and 20.7 km length. The left end of the slope is 5 m below,  
 276 and the right end 2.5 m above the reference water level, see figure 6a. The  
 277 Dirichlet boundary condition  $\eta_D$  controls the water level on the left domain  
 278 boundary, and a no-normal flow is enforced on the other boundaries.

279 The remaining parameters are  $g = 9.81 \text{ m/s}^2$  for the gravity constant and  
 280  $\mu = 0.025 \text{ s/m}^{1/3}$  for the Manning drag coefficient. The domain is uniformly  
 281 discretised with triangular elements of 1.2 km size, see figure 6b. For this  
 282 mesh, the guideline equation for the smoothness parameter (5) suggests a  
 283 value of  $\alpha = 0.43 \text{ m}$ . The time step is set to  $\Delta t = 600 \text{ s}$  and the final time  
 284 is  $T = 24 \text{ h}$ .

285 The model inputs to be reconstructed by the data assimilation are chosen  
 286 to be the free-surface displacement values on left boundary for each time level,  
 287 except during the final 2 h. The final 2 h cannot be reconstructed because  
 288 the boundary values have no influence on the wet/dry interface due to the  
 289 finite wave speed. This yields a total of 133 boundary values that need to be  
 290 reconstructed.

291 *4.1.1. Sinusoidal wave profile without noisy observations*

292 In a first experiment, the reference Dirichlet boundary  $\eta_D^{\text{exact}}$  consists of  
 293 one sinusoidal wave with  $p := 12$  h period and 1 m amplitude (figure 7a):

$$\eta_D^{\text{exact}}(t) := \begin{cases} 0 & \text{if } t < 6 \text{ h,} \\ \frac{1}{2} \left( -\cos \left( \frac{2\pi(t-6 \text{ h})}{p} \right) + 1 \right) & \text{if } 6 \text{ h} \leq t \leq 18 \text{ h,} \\ 0 & t > 18 \text{ h.} \end{cases} \quad (21)$$

294 The observations  $d$  in the goal quantity (12) are generated by solving the  
 295 shallow water model with these boundary values for 24 h and recording the  
 296 wet/dry interface  $\mathcal{H}(\eta - h)$  at every time level. The resulting observations  
 297 with  $\alpha = 0.43$  m are plotted in figure 7b.

298 To verify that the reference Dirichlet boundary condition  $\eta_D^{\text{exact}}$  combined  
 299 with these observations is indeed a solution to the optimisation problem (13),  
 300 the optimisation algorithm was executed with regularisation coefficient  $\beta = 0$   
 301 and  $\eta_D = \eta_D^{\text{exact}}$  as an initial guess. As expected, the algorithm terminated  
 302 after the first iteration, reporting that the first-order optimality conditions  
 303 hold, that is the gradient of the goal quantity is zero.

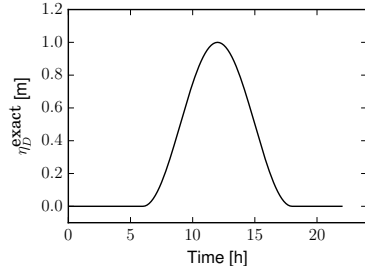
304 Next it was tested if the reference Dirichlet boundary condition can be  
 305 reconstructed without prior information. For that, the optimisation prob-  
 306 lem (13) was solved with  $\beta = 0$  and an initial guess of  $\eta_D = 0$ . The optimi-  
 307 sation algorithm was terminated once the relative change of the functional  
 308 value in one optimisation iteration dropped below  $10^{-9}$ . With that setup, the  
 309 optimisation finished after 17 iterations, see figure 7d. Figure 7c shows that  
 310 the reference Dirichlet condition was accurately reconstructed. The maxi-  
 311 mum discrepancy of the incoming wave profile is 0.1 cm, which corresponds  
 312 to a relative reconstruction error of 0.1 %.

313 The speed performance of the reconstruction can be measured by the ratio  
 314 between one reconstruction and one simulation. Of particular interest is to  
 315 test if this ratio increases when the number of control variables increases.  
 316 Therefore, we repeated the reconstruction for different temporal resolutions  
 317 ( $\Delta t = 600$  s, 300 s, 150 s) and measured the number of optimisation iterations,  
 318 runtime and the above-mentioned ratio. The results are listed in table 2  
 319 and confirm that the performance is independent of the number of control  
 320 variables.

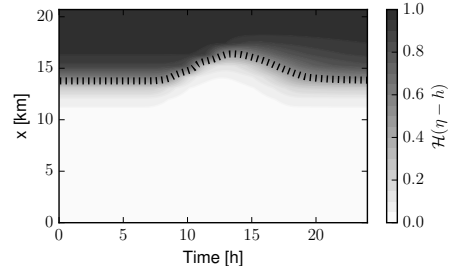
321 To test the impact of the smoothing parameter we increased  $\alpha$  from 0.43 m  
 322 to 1.8 m. The results are shown in figure 8. Compared to the previous ex-  
 323 periment, the smoother gradient at the wet/dry interface can clearly be seen.

$\Delta t$ (s)	Ctrl. var.	Opt. iters.	Runtime (s)	Opt./sim.
600	133	17	3,312	84
300	265	15	5,889	77
150	529	16	12,662	78

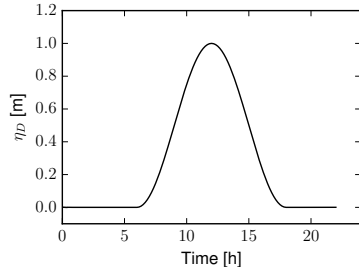
Table 2: Computational cost of the reconstruction problem described in 4.1.1 with varying temporal resolution.  $\Delta t$  denotes the time step, *Ctrl. var.* the number of control variables, *Opt. iters.* the number of optimisation iterations until convergence, *Runtime (s)* the total runtime for the optimisation and *Opt./sim.* the runtime ratio of the optimisation versus a single simulation.



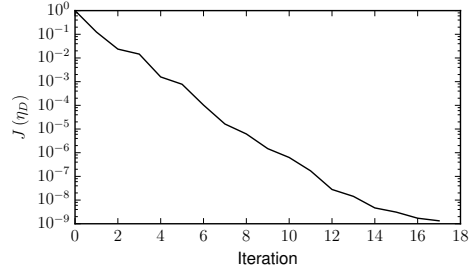
(a) Reference wave profile



(b) Observations and exact wet/dry interface (dashed line)



(c) Reconstructed wave profile



(d) Optimisation convergence

Figure 7: Results of the noiseless wave profile reconstruction on a sloping beach with a sinusoidal incoming wave profile and smoothing value  $\alpha = 0.43$  m. The final 2 h of the wave profile are excluded from the reconstruction.

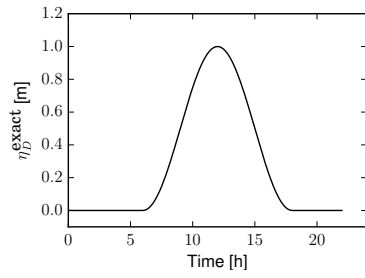
324 With this setup, the optimisation algorithm terminated after 14 iterations  
 325 and reconstructed the incoming wave profile up to a maximum error of less  
 326 than 0.03 cm. Overall, the reconstruction seems to work well for different  $\alpha$   
 327 values, however, a large smoothing constant can cause unphysical results as  
 328 described in Kärnä et al. (2011).

#### 329 4.1.2. Sinusoidal wave profile with noisy observations

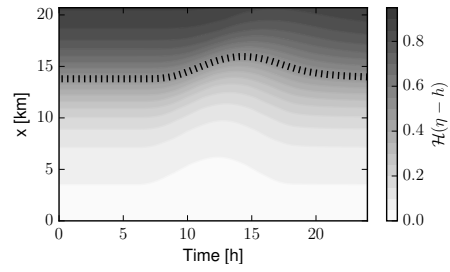
330 So far the experiments were performed with perfect observations in the  
 331 sense that the same model was used to produce the observations and to  
 332 reconstruct the wave profile. To avoid this ‘inverse crime’, we repeated the  
 333 experiment as described in 4.1.1 with  $\alpha = 0.43$ , but with pointwise Gaussian  
 334 noise added to the observations  $d$ . The noisy observations are shown on the  
 335 upper frames of figure 9 for two different noise levels. The impact of the  
 336 noise on the observations is clearly visible.

337 With noisy observations it becomes important to regularise the problem  
 338 in order to avoid the model describing the noisy data rather than the phys-  
 339 ical relationships, also known as overfitting. For comparison, we repeated  
 340 the reconstruction for three different regularisation values:  $\beta = 4 \times 10^9, 4 \times$   
 341  $10^{10}, 4 \times 10^{11}$ . These were chosen such that the functional terms are approx-  
 342 imately of the same magnitude at the beginning of the optimisation. The  
 343 results are shown in figure 9. The quality of the reconstructed wave profiles  
 344 depends clearly on the regularisation term. The larger  $\beta$  is, the smoother  
 345 and flatter the wave profile becomes. Considering the reference wave profile  
 346 10a, a value of  $\beta = 4 \times 10^{10}$  yields robust results for both noise levels in this  
 347 example.

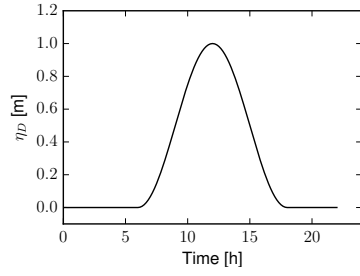
348 An open question is how to choose the regularisation parameter for new  
 349 problems effectively. A unit comparison on (12) reveals that the unit of  $\beta$   
 350 has the unit  $m^2s$  which suggests that  $\beta$  should scale with the domain area  
 351 and the simulation time interval  $T$ . An alternative, algorithmic approach  
 352 for choosing  $\beta$  is the discrepancy principle Morozov (1966); Hansen (1998);  
 353 Bonesky (2009), which selects the regularisation parameter such that the  
 354 perturbation of the regularisation term affects the solution with the same  
 355 order of the discrepancy induced by the noise, or the computationally more  
 356 efficient approach proposed by D’Elia et al. (2012b,a). A detailed study on  
 357 the choice of parametrisation value would be an interesting further study.



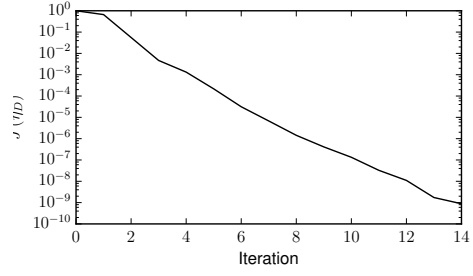
(a) Reference wave profile



(b) Observations and exact wet/dry interface (dashed line)



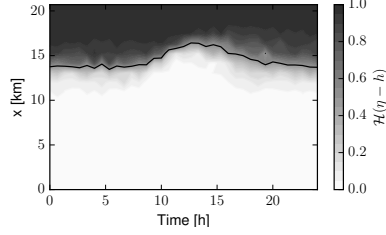
(c) Reconstructed wave profile



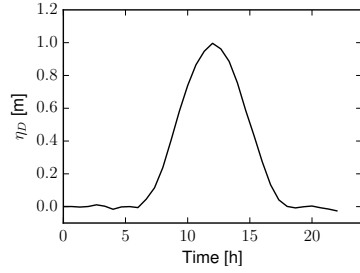
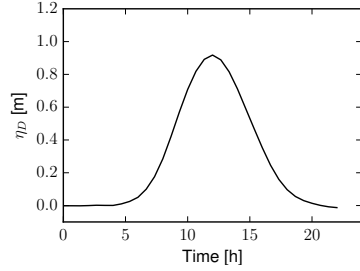
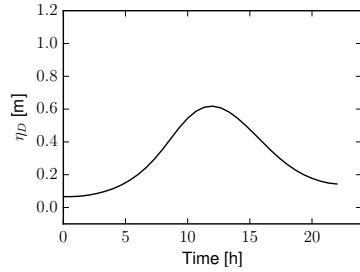
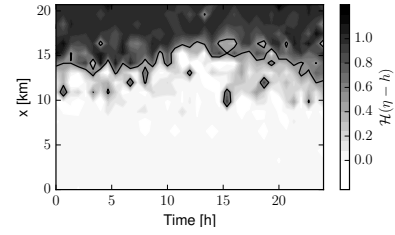
(d) Optimisation convergence

Figure 8: Results of the noiseless wave profile reconstruction on a sloping beach with a sinusoidal incoming wave profile and smoothing value  $\alpha = 1.8$  m. The final 2 h of the wave profile are excluded from the reconstruction.



a)  $\sigma = 0.1$ 

Observations and wet/dry interface

Reconstructed wave,  $\beta = 4.0 \cdot 10^9$ Reconstructed wave,  $\beta = 4.0 \cdot 10^{10}$ Reconstructed wave,  $\beta = 4.0 \cdot 10^{11}$ b)  $\sigma = 0.5$ 

Observations and wet/dry interface

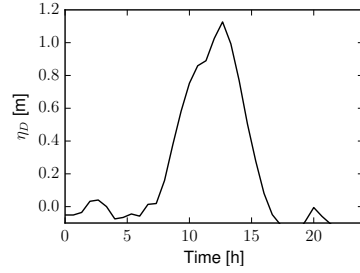
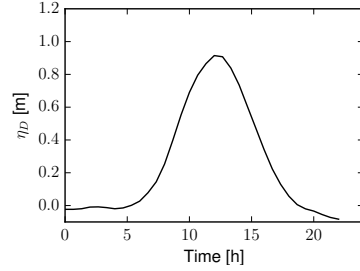
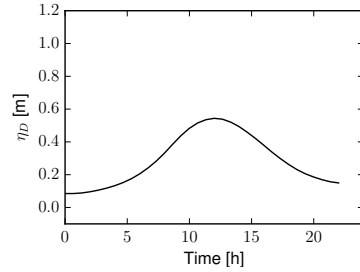
Reconstructed wave,  $\beta = 4.0 \cdot 10^9$ Reconstructed wave,  $\beta = 4.0 \cdot 10^{10}$ Reconstructed wave,  $\beta = 4.0 \cdot 10^{11}$ 

Figure 9: Results of the wave profile reconstruction on a sloping beach with a sinusoidal incoming wave profile, a smoothing value  $\alpha = 0.43$  m and pointwise Gaussian noise added to the observations with standard deviation  $\sigma = 0.1$  (left) and  $\sigma = 0.5$  (right). Different regularisation values  $\beta$  were used to control the smoothness of the reconstructed wave. The final 2 h of the wave profile are excluded from the reconstruction.

### 358 4.1.3. *Composed sinusoidal wave profile*

The next experiment demonstrates that a more complex wave profile can be reconstructed. For that, the previous example is repeated with a reference Dirichlet function  $\eta_D^{\text{exact}}$  that is the composition of two sinusoidal functions with different periods (figure 10a):

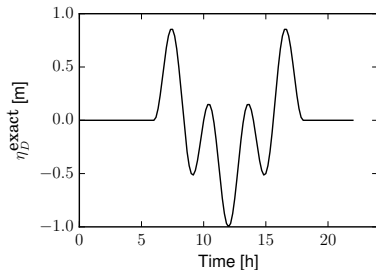
$$\eta_D^{\text{exact}}(t) = \begin{cases} 0 & \text{if } t < 6 \text{ h,} \\ \frac{1}{2} \left( \cos \left( \frac{2\pi(t-6 \text{ h})}{p} \right) - \cos \left( \frac{8\pi(t-6 \text{ h})}{p} \right) \right) & \text{if } 6 \text{ h} \leq t \leq 18 \text{ h,} \\ 0 & t > 18 \text{ h.} \end{cases}$$

359 where  $p := 12 \text{ h}$ . The smoothing value is again  $\alpha = 0.43 \text{ m}$ . The observa-  
 360 tions are generated in the same way as in example 4.1.1 and are plotted in  
 361 figure 10b.

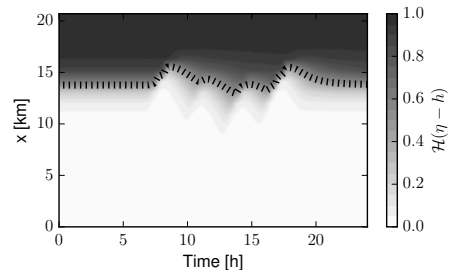
362 In this case, the optimisation tolerance was reached after 141 iterations.  
 363 The results in figure 10 show that the wave was successfully reconstructed.  
 364 The maximum error is 1.2 cm, or a relative error of 1.2 %. Comparing the  
 365 required numbers of iterations to the previous experiments indicates that  
 366 the shape/complexity of the wave profile to be reconstructed impacts the  
 367 convergence rate of the optimisation method. The exact mechanism for this  
 368 is not yet understood, but it may be related to the spectrum of the Hessian  
 369 at the minimiser.

### 370 4.2. *Reconstruction of the Hokkaido-Nansei-Oki tsunami wave profile*

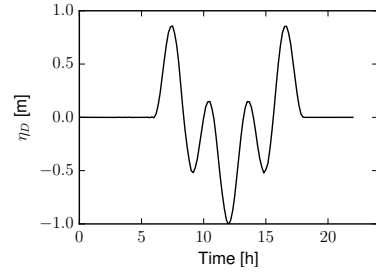
371 The second data assimilation problem is motivated by the question of  
 372 whether it is possible to reconstruct a tsunami wave profile from satellite  
 373 observations that record the inundation line over time. The considered event  
 374 is the Hokkaido-Nansei-Oki tsunami that occurred in 1993 and produced run-  
 375 up heights of up to 30 m on Okushiri island, Japan. The Central Research  
 376 Institute for Electric Power Industry (CRIEPI) in Abiko, Japan constructed  
 377 a 1/400 scale laboratory model of the area around the island (Matsuyama and  
 378 Tanaka, 2001). Following Yalciner et al. (2011), this experiment is simulated  
 379 in a rectangular domain of size  $5.448 \text{ m} \times 3.402 \text{ m}$ . The bathymetry and  
 380 coastal topography is shown in figure 11a. It contains an island in the centre  
 381 and coastal regions on the top right of the domain. On the left boundary  
 382 a surface elevation profile is enforced that resembles a tsunami wave (figure  
 383 12b). The aim of this experiment is to reconstruct this wave profile. On the  
 384 remaining boundaries, a no-normal flow condition is imposed.



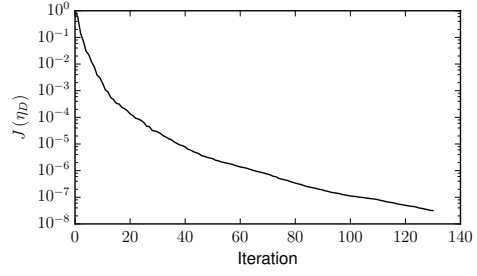
(a) Reference Dirichlet wave profile



(b) Observations and exact wet/dry interface (dashed line)



(c) Reconstructed wave profile



(d) Optimisation convergence

Figure 10: Results of the wave profile reconstruction on a sloping beach with a composed sinusoidal incoming wave profile and smoothing value  $\alpha = 0.43$  m. The final 2 h of the wave profile are excluded from the reconstruction.

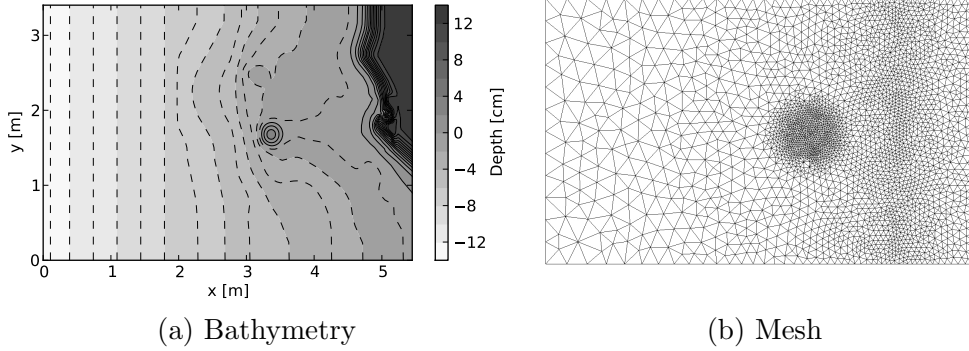


Figure 11: The laboratory setup of the Hokkaido-Nansei-Oki tsunami example, based on 1/400 laboratory experiment by the Central Research Institute for Electric Power Industry. The island at the centre and the coast on the right are hit by a tsunami shaped wave coming from the left boundary.

385 The domain is discretised with an unstructured mesh consisting of 5,730  
386 triangular elements with increasing resolution near the inundation areas, see  
387 figure 11b. The mesh elements size range from 0.4 m to 0.02 m. The tem-  
388 poral discretisation uses a time step of 0.5 s with a total simulation time  
389 of 32 s. The Manning coefficient is set to  $\mu = 0.025 \text{ s/m}^{\frac{1}{3}}$ . The observa-  
390 tions are synthetically generated by running the shallow water model with  
391 the reference wave profile used in the laboratory experiment while recording  
392 the wet/dry interface. No noise was added, and  $\beta = 0$  used. The smoothing  
393 guideline equation (5) yields  $\alpha \approx 0.16 \text{ m}$ , in the experiments we chose a value  
394 of  $\alpha = 0.1 \text{ m}$ .

395 The optimisation was initialised with a wave profile of  $1.05 \times 10^{-3} \text{ m}$  for  
396 all time levels, which corresponds to the final free-surface displacement of the  
397 input wave. For the same reason as in the examples above, the final 2 s of the  
398 Dirichlet boundary values were then reset to the reference Dirichlet boundary  
399 values and excluded from the reconstruction. Furthermore, a box constraint  
400 was used to restrict the minimum and maximum free-surface displacement  
401 to  $-1.5 \text{ cm}$  and  $+2 \text{ cm}$ , knowing that the reconstructed values is within  
402 this range. These constraints avoid unrealistically large Dirichlet boundary  
403 values at intermediate optimisation iterations for which the Newton solver in  
404 the shallow water model diverges. An alternative approach is to regularise  
405 with  $\beta > 0$ , but has the side effect that the reconstructed wave depends on  
406 the  $\beta$  value, see section 4.1.2.

407 The optimisation iteration converged after 67 iterations. The results are

408 shown in figure 12. The incoming wave was reconstructed up to an absolute  
409 error of  $9 \times 10^{-4}$  cm, or a relative error of less than  $6 \times 10^{-4}\%$ .

## 410 5. Summary

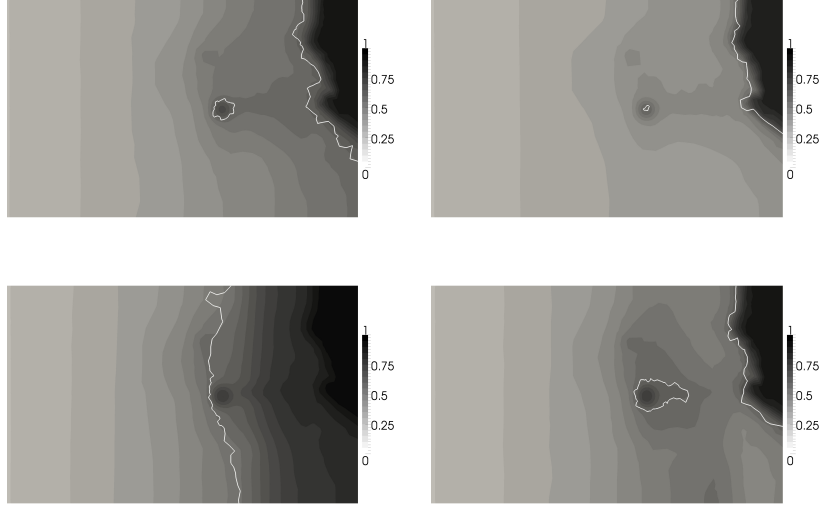
411 A shallow water model with wetting and drying and its adjoint model  
412 has been developed and used to reconstruct an incoming wave profile from  
413 inundation observations. The reconstruction is formulated as an optimisa-  
414 tion problem which minimises the difference between the observed and the  
415 simulated wet/dry interface and solved with an efficient gradient-based op-  
416 timisation method. This problem setup is a step towards reconstructing  
417 unknowns such as the tsunami source and wave profile from real inundation  
418 data that is available from historical data or satellite imaging.

419 Numerical experiments demonstrate that, under idealised conditions, the  
420 profile of the incoming wave can be accurately recovered. Furthermore, an  
421 experiment with added Gaussian noise in the observations showed robustness  
422 with respect to noisy data. However, multiple question remain unanswered.  
423 In particular, we lack convergence analysis for the regularised continuous  
424 problem to the nonsmooth, free-boundary problem. Similarly, convergence  
425 analysis of the discretisation of the regularised continuous problem is lacking.  
426 Furthermore, a mesh-independent optimisation method should be employed  
427 to obtain improve performance, in particular for setups with spatially vary-  
428 ing wave profiles or adaptive-timestepping. Finally, experiments with real  
429 observations are needed to fully exclude inverse crimes.

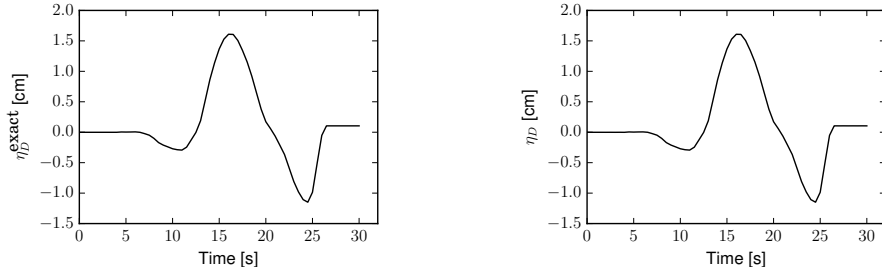
430 The initial results of the paper are promising and motivate future re-  
431 search in this direction: for example, the robustness of the data assimilation  
432 should be tested against partially missing observations. In this case, the  
433 regularisation parameter  $\beta$  will play an important role to enforce smooth-  
434 ness of the reconstructed wave profile. Another direction is to overcome  
435 the shallow water assumption, as it might not accurately capture important  
436 physical processes. One possibility is to replace the shallow water model with  
437 a three-dimensional wetting and drying model.

## 438 Code availability

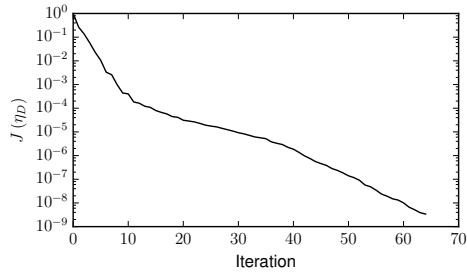
439 The model implementation and files needed to reproduce the results  
440 of this paper are freely available on bitbucket: <https://bitbucket.org/>



(a) The wet/dry interface observations after 0 s, 20 s, 29 s, 32 s, in reading order. The observations are constructed by running the forward problem with the synthetic Dirichlet boundary values. The observations are approximated indicator functions of the wet/dry interface (marked as white lines)



(b) The reference tsunami wave profile. (c) The reconstructed tsunami wave profile.



(d) The functional values during the optimisation iterations

441 `simon_funke/wetting_and_drying_optimisation_code`. The website con-  
442 tains a Readme file with instructions for how to install the software and  
443 reproduce the results of the paper.

## 444 Acknowledgements

445 This work was supported by the Grantham Institute for Climate Change,  
446 the Research Council of Norway through a Centres of Excellence grant to the  
447 Center for Biomedical Computing at Simula Research Laboratory (project  
448 number 179578), a FRIPRO grant (project number 251237), a UK Engineer-  
449 ing and Physical Sciences Research Council grant (EP/K030930/1) and a  
450 UK Natural Environment Research Council grant (NE/K000047/1).

## 451 References

- 452 Ascher, U. M., Ruuth, S. J., Spiteri, R. J., 1997. Implicit-explicit Runge-  
453 Kutta methods for time-dependent partial differential equations. *Applied*  
454 *Numerical Mathematics* 25 (2-3), 151–167.
- 455 Bagchi, A., Brummelhuis, P. T., 1994. Parameter identification in tidal mod-  
456 els with uncertain boundaries. *Automatica* 30 (5), 745–759.
- 457 Balzano, A., 1998. Evaluation of methods for numerical simulation of wetting  
458 and drying in shallow water flow models. *Coastal Engineering* 34 (1-2), 83–  
459 107.
- 460 Barros, M. L. C., Rosman, P. C. C., Telles, J. C. F., 2015. An effective  
461 wetting and drying algorithm for numerical shallow water flow models.  
462 *Journal of the Brazilian Society of Mechanical Sciences and Engineering*  
463 37 (3), 803–819.
- 464 Blaise, S., St-Cyr, A., Mavriplis, D., Lockwood, B., 2013. Discontinuous  
465 Galerkin unsteady discrete adjoint method for real-time efficient tsunami  
466 simulations. *Journal of Computational Physics* 232 (1), 416 – 430.
- 467 Bonesky, T., 2009. Morozov’s discrepancy principle and tikhonov-type func-  
468 tionals. *Inverse Problems* 25 (1), 015015.
- 469 Byrd, R. H., Lu, P., Nocedal, J., Zhu, C., 1995. A limited memory algo-  
470 rithm for bound constrained optimization. *SIAM Journal on Scientific and*  
471 *Statistical Computing* 16 (5), 1190–1208.

- 472 Cacuci, D. G., 1981. Sensitivity theory for nonlinear systems. i. nonlinear  
473 functional analysis approach. *Journal of Mathematical Physics* 22 (12),  
474 2794–2802.
- 475 Candy, A., 2017. An implicit wetting and drying approach for non-  
476 hydrostatic baroclinic flows in high aspect ratio domains. *Advances in*  
477 *Water Resources* 102, 188 – 205.
- 478 Chen, X., Navon, I. M., 2009. Optimal control of a finite-element limited-area  
479 shallow-water equations model. *Studies in Informatics and Control* 18 (1),  
480 41–62.
- 481 Comblen, R., Lambrechts, J., Remacle, J. F., Legat, V., 2010. Practical  
482 evaluation of five partly discontinuous finite element pairs for the non-  
483 conservative shallow water equations. *International Journal for Numerical*  
484 *Methods in Fluids* 63 (6), 701–724.
- 485 Cotter, C. J., Ham, D. A., Pain, C. C., 2009. A mixed discontinu-  
486 ous/continuous finite element pair for shallow-water ocean modelling.  
487 *Ocean Modelling* 26 (1-2), 86–90.
- 488 Courtier, P., Talagrand, O., 1990. Variational assimilation of meteorological  
489 observations with the direct and adjoint shallow-water equations. *Tellus*  
490 42 (5), 531–549.
- 491 de Brye, B., de Brauwere, A., Gourgue, O., Delhez, E. J., Deleersnijder, E.,  
492 2012. Water renewal timescales in the scheldt estuary. *Journal of Marine*  
493 *Systems* 94, 74 – 86.
- 494 de Brye, B., de Brauwere, A., Gourgue, O., Krn, T., Lambrechts, J.,  
495 Comblen, R., Deleersnijder, E., 2010. A finite-element, multi-scale model  
496 of the scheldt tributaries, river, estuary and {ROFI}. *Coastal Engineering*  
497 57 (9), 850 – 863.
- 498 D’Elia, M., Mirabella, L., Passerini, T., Perego, M., Piccinelli, M., Vergara,  
499 C., Veneziani, A., 2012a. Applications of variational data assimilation in  
500 computational hemodynamics. Springer Milan, pp. 363–394.
- 501 D’Elia, M., Perego, M., Veneziani, A., 2012b. A variational data assimilation  
502 procedure for the incompressible Navier-Stokes equations in hemodynam-  
503 ics. *Journal of Scientific Computing* 52 (2), 340–359.



504 Ding, Y., Wang, S., 2006. Optimal control of open-channel flow using adjoint  
505 sensitivity analysis. *Journal of Hydraulic Engineering* 132 (11), 1215–1228.

506 Ding, Y., Wang, S. S. Y., 2005. Identification of Manning’s roughness coeffi-  
507 cients in channel network using adjoint analysis. *International Journal of*  
508 *Computational Fluid Dynamics* 19 (1), 3–13.

509 Errico, R. M., 1997. What is an adjoint model? *Bulletin of the American*  
510 *Meteorological Society* 78 (11), 2577–2591.

511 Fang, F., Pain, C., Navon, I., Cacuci, D., Chen, X., 2013. The independent  
512 set perturbation method for efficient computation of sensitivities with ap-  
513 plications to data assimilation and a finite element shallow water model.  
514 *Computers & Fluids* 76, 33 – 49.

515 Farrell, P. E., Ham, D. A., Funke, S. W., Rognes, M. E., 2013. Automated  
516 derivation of the adjoint of high-level transient finite element programs.  
517 *SIAM Journal on Scientific Computing* 35 (4), C369–C393.

518 Funke, S. W., 2012. The automation of PDE-constrained optimisation and  
519 its applications. Ph.D. thesis, Imperial College London, London, UK.

520 Funke, S. W., Pain, C. C., Kramer, S. C., Piggott, M. D., 2011. A wetting  
521 and drying algorithm with a combined pressure/free-surface formulation  
522 for non-hydrostatic models. *Advances in Water Resources* 34 (11), 1483–  
523 1495.

524 Gejadze, I. Y., Copeland, G. J. M., 2005. Adjoint sensitivity analysis for  
525 fluid flow with free surface. *International Journal for Numerical Methods*  
526 *in Fluids* 47 (8-9), 1027–1034.

527 Geuzaine, C., Remacle, J.-F., 2009. Gmsh: A 3-D finite element mesh gener-  
528 ator with built-in pre- and post-processing facilities. *International Journal*  
529 *for Numerical Methods in Engineering* 79 (11), 1309–1331.

530 Gourgue, O., 2011. Finite element modeling of sediment dynamics in the  
531 Scheldt. Ph.D. thesis, École Polytechnique de Louvain, Belgium.

532 Gunzburger, M. D., 2003. *Perspectives in Flow Control and Optimization.*  
533 *Advances in Design and Control.* SIAM, Philadelphia, PA, USA.

- 534 Hairer, E., Wanner, G., 1996. Solving ordinary differential equations. II,  
535 volume 14 of Springer Series in Computational Mathematics. Springer-  
536 Verlag, Berlin,.
- 537 Hansen, P. C., 1998. Rank-deficient and discrete ill-posed problems: numer-  
538 ical aspects of linear inversion. Vol. 4. SIAM.
- 539 Hervouet, J.-M., 2007. Hydrodynamics of Free Surface Flows. John Wiley &  
540 Sons, Ltd, Ch. 2, pp. 5–75.
- 541 Hesthaven, J. S., Warburton, T., 2008. Nodal discontinuous Galerkin meth-  
542 ods: Algorithms, analysis, and applications. Vol. 54. Springer-Verlag,  
543 Berlin, Heidelberg, New York.
- 544 Hinze, M., Pinnau, R., Ulbrich, M., Ulbrich, S., 2009. Optimization with  
545 PDE constraints. Vol. 23 of Mathematical Modelling: Theory and Appli-  
546 cations. Springer-Verlag, Berlin, Heidelberg, New York.
- 547 Jones, E., Oliphant, T., Peterson, P., et al., 2001. SciPy: Open source scien-  
548 tific tools for Python.  
549 URL <http://www.scipy.org>
- 550 Kärnä, T., de Brye, B., Gourgue, O., Lambrechts, J., Comblen, R., Legat, V.,  
551 Deleersnijder, E., 2011. A fully implicit wetting–drying method for DG-  
552 FEM shallow water models, with an application to the Scheldt estuary.  
553 Computer Methods in Applied Mechanics and Engineering 200 (5–8), 509  
554 – 524.
- 555 Kawahara, M., Kawasaki, T., 1990. A flood control of dam reservoir by conju-  
556 gate gradient and finite element methods. In: Mori, K. (Ed.), Proceedings  
557 of the Fifth International Conference on Numerical Ship Hydrodynamics.  
558 The National Academies Press, Washington, D.C., USA, pp. 45–56.
- 559 Kowalik, Z., Knight, W., Logan, T., Whitmore, P., 2005. Numerical modeling  
560 of the global tsunami: Indonesian tsunami of 26 December 2004. Science  
561 of Tsunami Hazards 23 (1), 40– 56.
- 562 Logg, A., Mardal, K.-A., Wells, G. N., et al., 2011. Automated Solution  
563 of Differential Equations by the Finite Element Method. Springer-Verlag,  
564 Berlin, Heidelberg, New-York.

- 565 Matsuyama, M., Tanaka, H., 2001. An experimental study of the highest  
566 runup height in the 1993 Hokkaido Nansei-Oki earthquake tsunami. In:  
567 National Tsunami Hazard Mitigation Program Review and International  
568 Tsunami Symposium (ITS 2001). pp. 879–889.
- 569 Medeiros, S. C., Hagen, S. C., 2013. Review of wetting and drying algorithms  
570 for numerical tidal flow models. *International Journal for Numerical Meth-*  
571 *ods in Fluids* 71 (4), 473–487.
- 572 Miyaoka, T., Kawahara, M., 2008. Optimal control of drainage basin con-  
573 sidering moving boundary. *International Journal of Computational Fluid*  
574 *Dynamics* 22 (10), 677–686.
- 575 Morozov, V. A., 1966. On the solution of functional equations by the method  
576 of regularization. In: *Soviet Math. Dokl.* Vol. 7. pp. 414–417.
- 577 Naumann, U., 2011. *The Art of Differentiating Computer Programs*. Society  
578 for Industrial and Applied Mathematics.
- 579 Navon, I. M., Zou, X., Derber, J., Sela, J., 1992. Variational data assimilation  
580 with an adiabatic version of the nmc spectral model. *Monthly Weather*  
581 *Review* 120 (7), 1433–1446.
- 582 Samizo, Y., Kawahara, M., 2011. Optimal control of shallow water flows using  
583 adjoint equation method. *Advanced Materials Research* 403-408, 466–469.
- 584 Sanders, B. F., Katopodes, N. D., 1996. Optimal control of sudden water  
585 release from a reservoir. In: English, M., Szollosi-Nagy, A. (Eds.), *Man-*  
586 *aging Water: Coping with Scarcity and Abundance*. San Francisco, USA,  
587 pp. 314–319.
- 588 Sanders, B. F., Katopodes, N. D., 2000. Adjoint sensitivity analysis for  
589 shallow-water wave control. *Journal of Engineering Mechanics* 126 (9),  
590 909–919.
- 591 Song, L., Zhou, J., Li, Q., Yang, X., Zhang, Y., 2011. An unstructured  
592 finite volume model for dam-break floods with wet/dry fronts over complex  
593 topography. *International Journal for Numerical Methods in Fluids* 67 (8),  
594 960–980.

- 595 Stewart, L. M., Dance, S., Nichols, N. K., 2013. Data assimilation with  
596 correlated observation errors: experiments with a 1-d shallow water model.  
597 *Tellus A* 65.
- 598 Thacker, W. C., 1981. Some exact solutions to the nonlinear shallow-water  
599 wave equations. *Journal of Fluid Mechanics* 107, 499–508.
- 600 Vater, S., Beisiegel, N., Behrens, J., 2015. A limiter-based well-balanced  
601 discontinuous galerkin method for shallow-water flows with wetting and  
602 drying: One-dimensional case. *Advances in Water Resources* 85, 1 – 13.
- 603 Westerink, J. J., Luetlich, R. A., Feyen, J. C., Atkinson, J. H., Dawson, C.,  
604 Roberts, H. J., Powell, M. D., Dunion, J. P., Kubatko, E. J., Pourtaheri,  
605 H., 2008. A basin- to channel-scale unstructured grid hurricane storm surge  
606 model applied to southern Louisiana. *Monthly Weather Review* 136 (3),  
607 833–864.
- 608 Xue, H., Du, Y., 2010. Implementation of a wetting-and-drying model in  
609 simulating the Kennebec–Androscoggin plume and the circulation in Casco  
610 Bay. *Ocean Dynamics* 60 (2), 341–357.
- 611 Yalciner, A. C., Imamura, F., Synolakis, C. E., 2011. Amplitude evolution  
612 and runup of long waves: Comparison of experimental and numerical data  
613 on a 3D complex topography. In: Liu, P. L., Yeh, H., Synolakis, C. (Eds.),  
614 *Advanced Numerical Models For Simulating Tsunami Waves And Runup*.  
615 World Scientific Publishing Company, Ch. 9, pp. 243–247.
- 616 Zhang, J., Lin, J., Sun, X., Chen, C., 2009. Application of an improved wet-  
617 ting and drying scheme in POM. In: *Proceedings of the 2009 International  
618 Conference on Energy and Environment Technology - Volume 02*. IEEE  
619 Computer Society, Washington, DC, USA, pp. 427–432.
- 620 Zhao, L., Guo, B., Li, T., Avital, E. J., Williams, J. J. R., 2014. A  
621 well-balanced explicit/semi-implicit finite element scheme for shallow wa-  
622 ter equations in dryingwetting areas. *International Journal for Numerical  
623 Methods in Fluids* 75 (12), 815–834, fLD-14-0027.  
624 URL <http://dx.doi.org/10.1002/flD.3919>